Metallophysics and Advanced Technologies
Металофіз. новітні технол.
Metallofiz. Noveishie Tekhnol.
2026, vol. 48, No. 5, pp. 483–493
https://doi.org/10.15407/mfint.48.05.0483
Reprints available directly from the publisher

PACS numbers: 61.72.Ff, 61.72.Mm, 64.75.Nx, 68.37.Hk, 68.37.Lp, 81.30.Mh, 82.80.Yc

The Effect of Hot Deformation in the α and α + β Phase Fields on the Microstructure and Precipitate Evolution of the Zr–Sn–Nb–Fe Alloy

A. W. Aldeen, D. Y. Mahdi, and M. S. Tuma

Department of Materials Engineering,
College of Engineering, University of Kufa,
Najaf, Iraq

The microstructure and precipitates' evolution after hot deformation of Zr–Sn–Nb–Fe samples in the α and α + β phases are investigated using transmission electron microscopy (TEM), energy dispersive x-ray spectroscopy (EDS), scanning electron microscopy (SEM), and electron backscatter diffraction (EBSD) accessories. The results show that the grain structure of the hot-deformed Zr–Sn–Nb–Fe-alloy samples is elongated along the thermal-deformation direction, forming a long, strip-like structure. Numerous recrystallized small grains and subgrain boundaries exist between these strips. The precipitated phases in the deformed samples with increasing temperature are primarily β-Zr, with minor amounts of β-Nb and $Zr(Fe, Nb)_2$, exhibiting a relatively uniform dispersion.

Key words: Zr–Sn–Nb–Fe alloy, hot deformation, microstructure, precipitate phase.

Еволюцію мікроструктури та преципітатів після гарячої деформації зразків Zr–Sn–Nb–Fe у фазах α й α + β досліджували за допомогою трансмісійної електронної мікроскопії (ТЕМ), енергодисперсійної рентґенівської спектроскопії (ЕДРС), сканувальної електронної мікроскопії (СЕМ) та дифракції зворотньо розсіяних (відбитих) електронів (ДЗРЕ). Результати

Corresponding author: Ali Wafaa Aldeen
E-mail: aliw.altalqani@uokufa.edu.iq

Citation: A. W. Aldeen, D. Y. Mahdi, and M. S. Tuma, The Effect of Hot Deformation in the α and α + β Phase Fields on the Microstructure and Precipitate Evolution of the Zr–Sn–Nb–Fe Alloy, *Metallofiz. Noveishie Tekhnol.*, **48**, No. 5: 483–493 (2026). DOI: 10.15407/mfint.48.05.0483

показують, що зерниста структура зразків гарячедеформованого стопу Zr–Sn–Nb–Fe є витягнутою вздовж напрямку термічної деформації, утворюючи довгу, смугоподібну структуру. Між цими смугами розташовані численні дрібні рекристалізовані зерна та межі субзерен. Фази, що виділяються в деформованих зразках із підвищенням температури, являють собою переважно β-Zr, з незначними кількостями β-Nb та $Zr(Fe, Nb)_2$, демонструючи відносно рівномірну дисперсію.

Ключові слова: стоп Zr–Sn–Nb–Fe, гаряча деформація, мікроструктура, фаза осаду.

(Received 11 February, 2026; in final version, 30 April, 2026)

1. INTRODUCTION

Zirconium alloys have long been widely used as fuel cladding materials for nuclear power reactors due to their advantages such as small neutron absorption cross-section, high thermal conductivity, and good resistance to waterside corrosion. As reactors develop towards high fuel consumption and long life, the in-core corrosion performance, hydrogen absorption performance, irradiation elongation, and creep performance of zirconium alloy cladding at high fuel consumption have become primary concerns. In the late 1970s, developed countries began to develop new zirconium alloy cladding materials and successively developed a series of new zirconium alloys, such as France's M5, the United States' ZIRLO, Russia's E635, Japan's DNA and MDA, and South Korea's HANA series alloys [1–4]. China has been conducting research on new zirconium alloys since the early 1990s. Through a series of studies, the composition of N36 zirconium alloy (Zr–1Sn–1Nb–0.3Fe) was determined, and industrial-scale pipe development work was carried out [5, 6].

Zirconium alloy preparing must undergo ingot melting, forging, homogenization, hot extrusion, annealing after hot extrusion, multiple cold rolling and intermediate annealing, cold rolling of finished products, and final annealing. Compared with Zr-4 alloy, the addition of Nb elements to N36 zirconium alloy reduces its $\alpha \rightarrow \alpha + \beta$ phase transformation temperature from about 810°C of Zr-4 alloy to below 680°C [7]. Therefore, the processing temperature of the new zirconium alloy should be reduced accordingly. In addition, when the Nb content is higher than 0.6%, Zr–Nb zirconium alloy will undergo segregation reaction at about 610°C, generating β-Zr [8–10]. In order to avoid the reduction of the corrosion resistance of the alloy due to the formation of β-Zr [11], the heat treatment of Zr–Nb alloy needs more practical fields to understand the segregation temperature and formation of precipitates.

This study used transmission electron microscopy (TEM), scanning

electron microscopy (SEM), and electron backscatter diffraction (EBSD) accessories to investigate the microstructure of Zr–Sn–Nb–Fe zirconium alloy plate hot-deformed at 600–750°C. The grain structure, grain boundary characteristics, and precipitation formation mechanism of the hot-deformed samples were analysed, providing a theoretical basis for subsequent processing.

2. EXPERIMENTAL/THEORETICAL DETAILS

2.1. Materials Sampling Method

In this study, the nominal composition of Zr–Sn–Nb–Fe zirconium alloy was Zr–1%Sn–1%Nb–0.3%Fe, and hot deformed was used at 600–750°C with strain rate 5 s^{-1} to investigate the microstructure evolution. Using SEM with its EBSD accessory and TEM, the specimens were observed along parallel ND–RD axis of the original plate (Fig. 1). The final diameter and height of the cylindrical samples used in this experiment was 6 mm. In order to be able to identify the RD observation area of the original plate on the sample after compression deformation, a small notch is left on the cylindrical surface to mark the RD of the plate.

2.2. Structural Characterization

The final diameter and height of the cylindrical samples used in this experiment was 6 mm. In order to be able to identify the RD observation area of the original plate on the sample after compression deformation, a small notch is left on the cylindrical surface to mark the RD of the plate. The Gleeble 3500 thermal simulation testing apparatus was used to finish the thermal compression experiment. EBSD samples were prepared using a vibratory polishing and chemical polishing method. The vibratory polisher was a BUEHLER VIBROMET2, and the

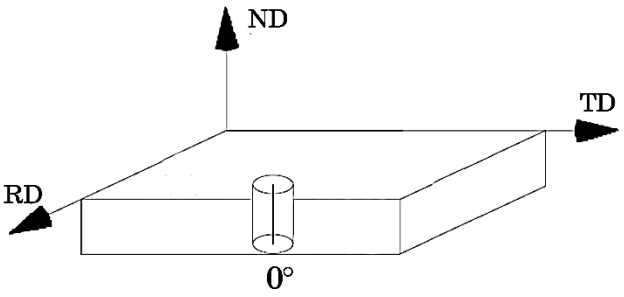

Fig. 1. Method of sampling from original plate.

chemical polishing solution was H_2SO_4:HNO_3:H_2O:HF = 15:30:45:6 (volume ratio). After chemical polishing, the samples were immediately rinsed with running water and alcohol. The prepared samples were characterized for microstructure using an EBSD system (HKL) equipped with a field emission scanning electron microscope (FEI NOVA NANO SEM 400). Electron beam scanning was used, with a typical scan step size of 0.1 μm and a scanning area of 150×150 points. HKL's CHANNEL-5 software was used for data analysis and microstructure reconstruction.

The precipitate phase was prepared using mechanical polishing and chemical etching. For observation, the sample was first polished to 5000# with sandpaper and then chemically etched using a solution of glycerol:nitric acid:hydrofluoric acid = 6:3:1 (volume ratio). After chemical polishing, it was immediately rinsed with running water. The surface was wiped clean with a clean cotton ball and ultrasonically cleaned in acetone for 3 minutes. The sample was then rinsed in 60°C concentrated nitric acid to remove polymeric substances adhering to the surface. The sample was then rinsed with running water and dried for later use. The morphology and composition of the precipitate phase were analysed using a FEI NOVA NANO SEM 400 with an EDS accessory. TEM samples were prepared using a mechanical thinning and electrolytic double-spray thinning method. The chemical thinning solution was $HClO_4$:CH_3CH_2OH = 11.5:86 (volume ratio). The prepared samples were analysed for grain structure and precipitated phases using a high-resolution transmission electron microscope.

3. RESULTS AND DISCUSSION

3.1. Grain Structure

Figure 2 shows the ND–RD plane EBSD reconstruction of the hot deformed samples at 600°C and 750°C. The analysis results show that the hot-deformed area exhibits a typical post-deformation locally dynamically recrystallized structure. Most of the grains are elongated, forming long strips approximately 20 μm long and 3 μm wide. These strips contain numerous subgrains, and most of the small grains have the same orientation or a small orientation difference. Locally, dynamically recrystallized grains are present, with an average grain size of approximately 0.5 μm. In addition, some grains show resistance to deformation process. Differences in hot deformation temperature led to variations in crystallographic orientation between the α and $\alpha+\beta$ phases in zirconium alloys, which are attributed to their distinct crystal structures, deformation mechanisms, and phase transformations governed by specific orientation relationships.

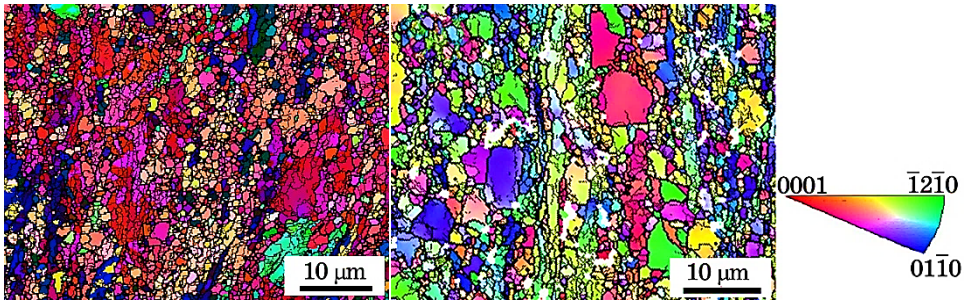

Fig. 2. EBSD Images of ND–RD observation area at 600°C (*a*), 750°C (*b*).

TEM analysis of hot deformed samples at different temperatures shows a trend that the structure consists primarily of two types of structures: lath-like structure and fine equiaxed recrystallized structure (Fig. 3, *a*). The laths contain a high density of dislocations (Fig. 3, *b*). The EBSD recrystallization positive polarity map of the hot-deformed sample also shows a small orientation difference between the deformed and recrystallized grains, indicating that dynamic recrystallization occurs through continuous subgrain boundary rotation (Fig. 4).

An average analysis of the EBSD grain boundary diagram reveals that this elongated microstructure contains high-density, small-angle grain boundaries surrounded by fine, equiaxed, dynamically recrystallized grains. There are two theories regarding its formation: the first one is the originally equiaxed grains, under high temperature and with suitable grain orientation and sufficient independent slip systems,

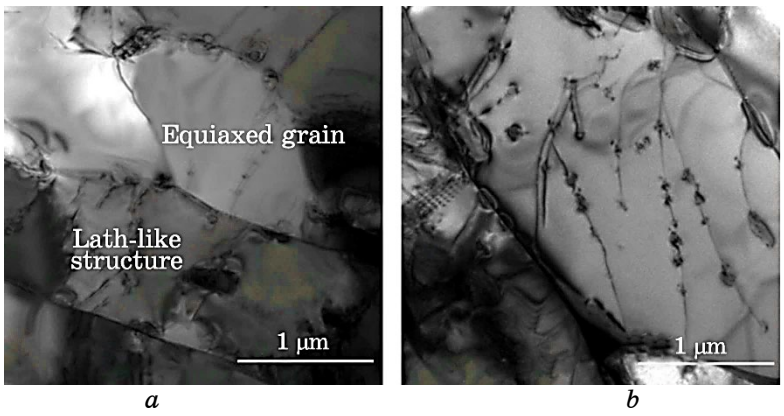

Fig. 3. TEM microstructure of deformed samples: lath and partial recrystallization structure (*a*); lath structure contains high density of dislocations (*b*).

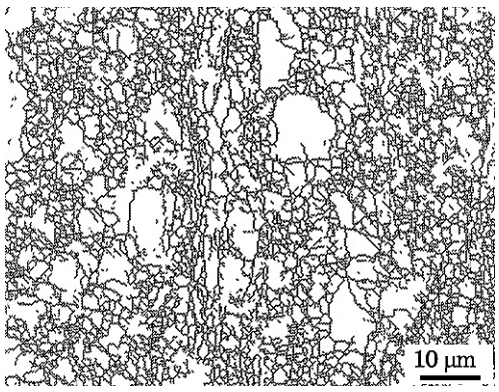

Fig. 4. EBSD grain boundaries map of hot deformed sample.

they can uniformly deform into elongated shapes, similar to the deformation of cubic metal grains; and the second one they are formed from original coarse equiaxed grains through continuous horizontal shearing and friction at high temperatures, with the large grains disappearing slowly and being partially retained [12–15]. Figure 4 shows that there are many subgrain boundaries within the large, elongated deformed grains, indicating that slip deformation also occurred within the elongated structure. The slip systems that zirconium alloys may excite at high temperatures mainly include the $\{10\bar{1}0\}<1\bar{2}10>$ cylindrical slip system, the $\{10\bar{1}0\}$ and $\{11\bar{2}1\}$ conical slip system, and can also be obtained through the $\{10\bar{1}2\}<\bar{1}011>$ twins promote the deformation of zirconium alloys, while the $\{10\bar{1}0\}<1\bar{2}10>$ and $\{10\bar{1}1\}<1\bar{2}10>$ slip systems can provide 2 and 4 independent slip systems [16, 17], respectively. This indicates that although Zr–Sn–Nb–Fe alloy has a relatively large number of independent slip systems at high temperatures, it still has fewer independent slip systems compared to cubic metals. On the other hand, from the perspective of orientation distribution, the orientation of the elongated structures is relatively close to that of the recrystallized equiaxed grains, both being slightly deflected tangential orientations, which are conducive to the activation of the $<\mathbf{a}>$ and $<\mathbf{a}+\mathbf{c}>$ slip systems [18]. This indicates that the original large grain orientations corresponding to these elongated structures are conducive to plastic deformation, while the distortion energy accumulated during the deformation process is relatively low. The original coarse grain orientations of other parts are not conducive to plastic deformation, and the distortion energy accumulated during the deformation process is relatively high.

Studies by K. Murty *et al.* have shown that under higher extrusion ratios, Zr–0.25Sn–1.0Nb–0.35Fe zirconium-alloy extrusion billets also exhibit similar elongated structures, while Zr-4 alloys all exhibit

fine equiaxed recrystallized structures. This indicates that the slower-diffusion Nb element may hinder the dynamic recrystallization of Zr–Sn–Nb–Fe zirconium alloys [19]. Therefore, during hot deformation, deformed structures with high distortion energy will become fine equiaxed dynamic grain structures due to dynamic recrystallization. The presence of Nb element hinders the dynamic recrystallization of some deformed structures with lower distortion energy, and the dislocations inside will merge to form small-angle grain boundaries or subgrain boundaries, still basically preserving the original grain structure the elongated tissue after deformation.

3.2. Precipitated Phase

SEM analysis showed that there were precipitates in the hot-deformed samples deformed at 600°C and 750°C (Fig. 5). Most precipitates which were distributed in a string-like pattern along the hot deformed direction, with an average size of more than 250 nm in an average. Most of the precipitates at 600°C are fine particles and the energy dispersive spectroscopy analysis shows that the mainly composed of Nb indicating high β-Nb precipitate percentage, and some of $Zr(Nb, Fe)_2$. At 750°C, the precipitate shows the same trend of elongated along the deformed direction, indicating that these precipitates have good plasticity. In niobium–zirconium alloys, except for the metallic β-Zr and β-Nb, the others are relatively hard and brittle intermetallic compound precipitates. β-Nb is generally finer. Energy dispersive spectroscopy analysis shows that most precipitates are mainly composed of Zr and a small amount of Fe and Nb. Considering that zirconium alloys with Nb content exceeding 0.6% will undergo segregation reaction at a certain temperature. Studies by Toffolon *et al.* have shown that the segrega-

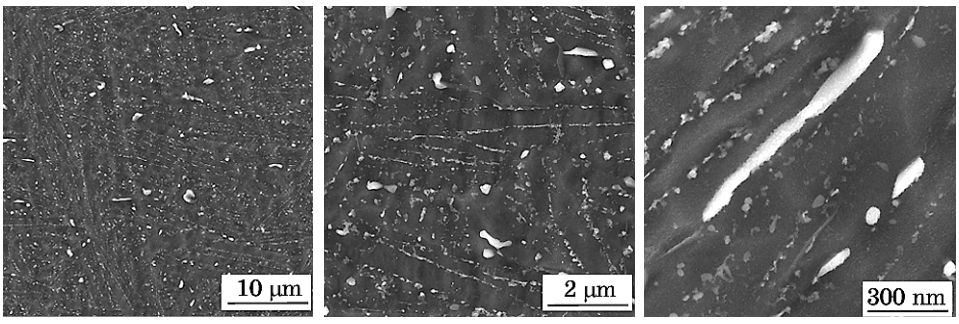

Fig. 5. SEM second phase particles image of hot deformed sample: low magnification at 600°C (*a*); high magnification at 600°C (*b*); sample deformed at 750°C (*c*).

tion temperature of Zr–1.0Nb is above 600°C, while studies by Hyun-Gil Kim *et al.* have shown that the segregation temperature of Zr–2.0Nb is approximately 585°C [8, 9]. However, the temperature during hot deformation of the Zr–Sn–Nb–Fe alloy in this study exceeds this temperature, allowing it to enter the $\alpha+\beta$ phase region. The β phase is likely to be retained at the end of deformation due to the rapid cooling rate. Therefore, the precipitates observed by SEM should almost be β-Zr.

TEM studies revealed that the precipitates in the hot-deformed samples were almost retained β-Zr structures at the grain boundaries (Fig. 6), and trace amounts of β-Nb and the $Zr(Fe, Nb)_2$ phase (Fig. 7). The Nb/Fe value in the $Zr(Fe, Nb)_2$ phase is relatively dispersed, ranging from about 0.1 to 15, while the Nb/Fe ratio in the Zr–Sn–Nb–Fe zirconium alloy containing the Nb and Fe second phase is generally in a smaller range [20–22]. This indicates that for primary products such as Zr–Sn–Nb alloy hot deformed samples, the distribution of alloying elements is not uniform. In addition to solid solutions in precipitates such as β-Zr and $Zr(Fe, Nb)_2$, a large number of alloying elements are supersaturated and solidly dissolved in the matrix, which is significantly different from a uniform equilibrium structure. A uniform equilibrium structure can be obtained through subsequent processing. K. Murty *et al.* study on Zr–0.25Sn–1.0Nb–0.35Fe zirconium alloy extrusion billets showed that the precipitates mainly consisted of harder intermetallic compound precipitates $Zr(Fe, Cr)_2$ and $(Zr, Nb)_4Fe_2$, as well as softer metallic precipitates β-Zr and β-Nb, *etc.* [19]. This indicates that even at lower deformation temperatures, Zr–Sn–Nb zirconium alloys may will produce β-Zr. Considering β-Zr and its string-like structures formed during subsequent processing, the adverse effects of distributed second-phase particles on the corrosion of zirconium al-

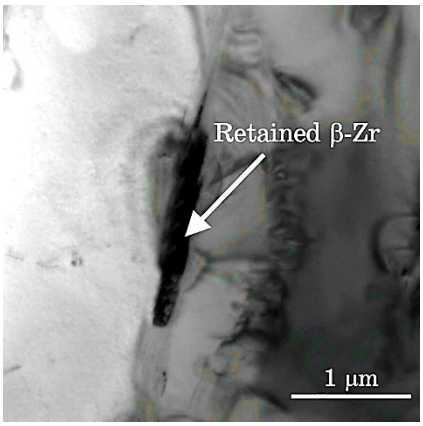

Fig. 6. Image of β-Zr precipitated in hot deformed samples.

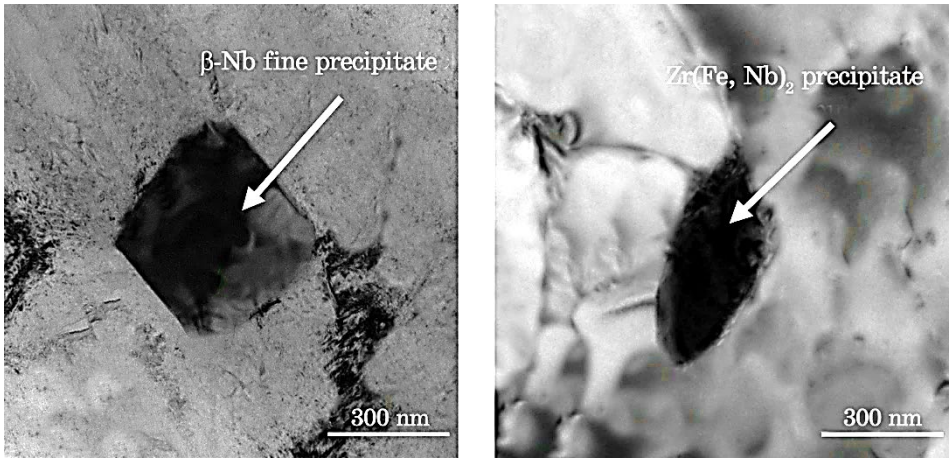

a *d*

Fig. 7. Image of precipitated β-Nb (*a*), $Zr(Fe, Nb)_2$ (*b*).

loy necessitate measures during subsequent processing to eliminate residual β-Zr and the formation of string-like second-phase distributions, resulting in a finely dispersed second-phase [21, 23]. Furthermore, considering that supersaturated Nb dissolved in the zirconium matrix also negatively impacts the corrosion resistance of zirconium alloys [24], Zr–Sn–Nb–Fe zirconium alloys should be deformed at the lowest possible temperature, with a larger rolling deformation and a lower annealing temperature to promote the full precipitation of Nb within the zirconium matrix, forming a finely dispersed second phase and improving the corrosion resistance of Zr–Sn–Nb–Fe zirconium alloys.

4. CONCLUSION

The results of studying microstructure and precipitates evolution of Zr–Sn–Nb–Fe alloy during hot deformation at α and α + β phase showed the following.

1. The alloy matrix is a mixture of lath-like structure and locally dynamically recrystallized fine-grained structure.
2. During deformation, most precipitates are distributed in a string-like pattern. At 600°C, fine particles with mainly composed of Nb indicate high β-Nb precipitate percentage, and some of $Zr(Nb, Fe)_2$. As temperature rises to the α + β two-phase region, residual β-Zr and trace amounts of β-Nb and $Zr(Fe, Nb)_2$ phases can be observed in the matrix.
3. This inhomogeneous microstructure negatively influences its corrosion resistance. Therefore, subsequent processing of Zr–Sn–Nb–Fe al-

loy should employ large deformation and low-temperature annealing processes to obtain a fine, dispersed second-phase microstructure, thereby improving the alloy corrosion resistance.

The authors gratefully acknowledge Baoji Five Elements Metal Co., Ltd, for the Zr alloy sheet. Special thanks to Mr. Erik Nilsson and Prof. Chen for their cooperation in this work.

AUTHORS' CONTRIBUTIONS

Ali W. Aldeen: methodology, validation, formal analysis, visualization, writing-original draft, review & editing, article structure construction. Dina Y. Mahdi: review & editing. Mohammed. S. Tuma: resources.

REFERENCES

1. B. O. Okonkwo, Z. Li, L. Li, J. Wang, and E.-H. Han, *Corros. Rev.*, **43**, Iss. 6: 609 (2024).
2. J. Hu and G. Cao, *Zirconium Alloy Coatings: Advances in Research and Applications* (Singapore: Springer Nature: 2025).
3. A. W. Aldeen, Z. W. Chen, I. A. Disher, M. Samiuddin, and K. Yan, *Phys. Met. Metallogr.*, **124**, No. 4: 362 (2023).
4. A. M. Garde, R. J. Comstock, G. Pan, R. Baranwal, L. Hallstadius, T. Cook, and F. Carrera, *Zirconium in the Nuclear Industry: 16th International Symposium* (Eds. M. Limbäck and R. Baranwal) (West Conshohocken, PA: ASTM International: 2012), **1529**, pp. 649–681.
5. C. Sun, Z. Yang, and Z. Wu, *World J. Nucl. Sci. Technol.*, **8**, No. 2: 30 (2018).
6. R. Qiu, B. Luan, L. Chai, X. Zhang, and Q. Liu, *Sci. China Technol. Sci.*, **56**, No. 1: 60 (2013).
7. W. Zhao, Y. Liu, H. Jiang, and Q. Peng, *J. Alloys Compd.*, **462**: 103 (2008).
8. C. Toffolon, J. Cristophe, and G, Jago, *ASTM Spec. Tech. Publ.*, **1423**: 361 (2002).
9. H.-G. Kim, J.-Y. Park, and Y.-H. Jeong, *J. Nucl. Mater.*, **347**, Nos. 1–2: 140 (2005).
10. R. Kondo, N. Nomura, Y. Tsutsumi, H. Doi, and T. Hanawa, *Acta Biomater.*, **7**, No. 12: 4278 (2011).
11. Y. P. Devi, H. Donthula, N. Keskar, A. Sarkar, K. Vaibhaw, and K. V. M. Krishna, *J. Nucl. Mater.*, **530**: 151978 (2020).
12. Y. Bi, B. Chen, L. Lu, and J. Yang, *Mater. Today Commun.*, **40**: 109524 (2024).
13. A. I. Dekhtyar, V. I. Bondarchuk, O. P. Karasevska, D. V Oryshych, D. G. Savvakin, and M. A. Skoryk, *Mater. Charact.*, **158**: 109949 (2019).
14. K. K. Saxena and V. Pancholi, *Met. Mater. Int.*, **27**, No. 7: 2106 (2021).
15. K. Saxena, V. Pancholi, G. Chaudhari, and D. Srivastava, *Mater. Sci. Forum*, **890**: 319 (2017).
16. A. Gaillac, C. Lemaignan, and P. Barberis, *Zirconium in the Nuclear Industry: 16th International Symposium* (Eds. M. Limbäck and R. Baranwal) (West Con-

shohocken, PA: ASTM International: 2012), **1529**, pp. 288–315.
17. E. Tenckhoff, *J. ASTM Int.*, **2**, No. 4: 1 (2005).
18. T. A. Hayes and M. E. Kassner, *Mechanical and Creep Behavior of Advanced Materials* (Ed. Linga Murty) (Springer: 2017), pp. 103–114.
19. K. L. Murty and I. Charit, *Prog. Nucl. Energy*, **48**, No. 4: 325 (2006).
20. A. V. Nikulina, V. A. Markelov, M. M. Peregud, Y. K. Bibilashvili, and V. A. Kotrekhov, *Zirconium in the Nuclear Industry: Eleventh International Symposium* (Eds. E. R. Bradley and G. P. Sabol) (West Conshohocken, PA: ASTM International: 1996), **1295**, pp. 785–804.
21. J. Huang, M. Yao, C. Gao, X. Liang, J. Peng, and J. Zhang, *Corros. Sci.*, **99**: 172 (2015).
22. C. Toffolon-Masclet, J.-C. Brachet, and G. Jago, *J. Nucl. Mater.*, **305**, Nos. 2–3: 224 (2002).
23. L. Chen, X. Song, H. Pang, and L. Liu, *Prog. Nucl. Energy*, **93**: 84 (2016).
24. B. D. C. Bell, S. T. Murphy, R. W. Grimes, and M. R. Wenman, *Acta Mater.*, **132**: 425 (2017).